Cluster description of cold (neutronless) α ternary fission of ^{252}Cf

A. Săndulescu,[1,2] F. Carstoiu,[1,2] I. Bulboacă,[1] and W. Greiner[2]

[1]*National Institute of Nuclear Physics and Engineering, P.O. Box MG-6, 76900 Bucharest-Magurele, Romania*
[2]*Institut für Theoretische Physik der J. W. Goethe Universität, D-60054, Frankfurt am Main, Germany*

A coplanar three body cluster model (two deformed fragments and an α particle) similar to the model used for the description of cold binary fission was employed for the description of cold (neutronless) α accompanied fission of ^{252}Cf. No preformation factors were considered. The three body potential was computed with the help of a double folding potential generated by the M3Y-NN effective interaction and realistic fragment ground state deformations. From the minimum action principle, the α particle trajectory equations, the corresponding ternary barriers, and an approximate WKB expression for the barrier penetrability are obtained. The relative cold ternary yields were calculated as the ratio of the penetrability of a given ternary fragmentation and the sum of the penetrabilities of all possible cold ternary fragmentations. Different scenarios were considered depending on the trajectories of the fragments. It was shown that two regions of cold fragmentation exist, a deformed one corresponding to large fragment deformations and a spherical one around ^{132}Sn, similarly to the case of the cold binary fission of ^{252}Cf. We have shown that for the scenario corresponding to the Lagrange point, where all forces acting on the α particle are in equilibrium, the cold α ternary yields of ^{252}Cf are strongly correlated with the cold binary yields of the daughter nucleus ^{248}Cm into the same heavy fragments. For all other scenarios only the spherical splittings are favored. We concluded that due to the present available experimental data on cold α ternary yields only the Lagrange scenario could describe the cold α ternary fission of ^{252}Cf. [S0556-2813(99)02610-2]

I. INTRODUCTION

The cold rearrangement of large groups of nucleons from the ground state of an initial nucleus to the ground or low excited states of two or three final fragments is now a well-established phenomenon [1–12]. The first direct evidence was the discovery of cluster radioactivity, i.e., the spontaneous emission of light nuclei such as α particles and heavier nuclei ranging from ^{14}C to ^{32}Si [2]. In such decays the Q_2-value principle, where Q_2 is the binary decay energy, dictates the most probable fragmentations since one fragment is the spherical nucleus ^{208}Pb or one close to it. The second direct evidence was the cold (neutronless) fission of many actinide nuclei into fragments with masses from $\simeq 70$ to $\simeq 160$ [3–10]. In these decays the fragment high rank static deformations, especially the hexadecupole ones, dictate the most probable fragmentations by lowering the barriers close to the Q_2 values [3]. In addition, a new region around the spherical ^{132}Sn nucleus may exist, where the Q_2-value principle dictates again the most probable fragmentations, similarly to cluster radioactivity [11,12]. It is worth mentioning that these decays were first observed indirectly by measuring the largest kinetic energy (TKE) of the fragments. For these cold (neutronless) decays the total excitation energy (TXE) is less than the binding neutron energy (B_n); i.e., the TKE is close to Q_2 [4,13]. The first direct observation of cold (neutronless) binary fragmentations in the spontaneous fission of ^{252}Cf was made [8,9] by using the multiple Ge-detector Compact Ball facility at ORNL and more recently with the Gammasphere consisting of 72 detectors [10].

The third direct evidence was the observation for the first time of cold (neutronless) α ternary fission yields [14]. The triple γ coincidence technique was used. Only the correla-

tions between the two heavier fragments were observed unambiguously. Recently ^{10}Be cold (neutronless) ternary fission was also observed unambiguously. This was possible by detecting the γ ray corresponding to the decay of the first 2^+ state in ^{10}Be in coincidence with the γ rays of the fission parteners ^{96}Sr and ^{146}Ba. It was shown that the yield to the first excited state in ^{10}Be for the ^{96}Sr-^{146}Ba split is of the order of 4.0×10^{-4} per 100 fission events [15]. These new phenomena are equivalent to cluster radioactivity during fission. Such cold ternary decays produce all three fragments with very low or zero internal excitation energy and consequently with very high kinetic energies. Their TKE will be close to the corresponding ternary decay energy Q_3. In order to achieve such large TKE values the three final fragments should have very compact shapes at the scission point and deformations close to those of their ground states, similarly to the case of cold binary fragmentations [16].

In this paper, a coplanar three cluster model consisting of two deformed fragments and a spherical α particle was employed for the description of cold (neutronless) α accompanied fission of ^{252}Cf. This model is similar to the cluster model used for the description of cluster radioactivity [2] or cold binary fission [3]. No preformation factors were included in our description. The three body potential was computed with the help of a double folding potential generated by the M3Y-NN effective interaction [10,16] and realistic fragment ground state deformations [17] as the sum of the interaction potentials between all three bodies. It is shown that this potential has two ridges: the α particle ridge defined by the α barrier around the two fragments and the interfragment ridge defined by the equilibrium of classical forces acting on the α particle, situated in the equatorial plane and disappearing for large distances between fragments. The in-

tersection of these two ridges gives the Lagrange point where no net forces are acting on the α particle. The interfragment ridge has a minimum on the fragment axis and a maximum at the Lagrange point. Such a potential structure suggests different initial positions of the α particle, all of them situated in the neighborhood of the equatorial plane, outside the interfragment axis: at the Lagrange point or in some quantum state in the interfragment well. In addition, the most intuitive configuration, i.e., the adiabatic configuration, is given by the α particle situated initially outside the interfragment axis, touching both fragments and tending to be collinear with the fragments when increasing the distance between them. Evidently this configuration must satisfy the equilibrium condition with both fragments.

From the minimum action principle, the α particle trajectories and the corresponding ternary barriers as a function of the interfragment distance are obtained. The WKB expression for the barrier penetrability in the presence of the α particle is also derived. It is shown that this expression involves an effective mass depending on the α particle trajectory.

The relative cold ternary yields were calculated for different initial positions of the α particle, i.e., different scenarios, as the ratio of the penetrability for a given ternary fragmentation and the sum of the penetrabilities for all possible cold ternary fragmentations. It was shown that two regions of cold fragmentation exist, a deformed region with large fragment deformations and a region around ^{132}Sn with at least one spherical fragment, similarly to the case of the cold binary fission of ^{252}Cf. The Lagrange scenario leads to cold α ternary yields of ^{252}Cf strongly correlated with the cold binary yields of the daughter nucleus ^{248}Cm. The adiabatic scenario strongly favors the spherical splittings, contrary to the presently available experimental data [14]. The ground and first excited state scenarios lead for spherical splittings to ternary barriers below the Q_3 values. For higher excited state scenarios, cold fission yields in both regions are obtained, but the yields for spherical splittings around ^{132}Sn are too large. Based on the present available experimental data on alpha ternary cold yields [14] it can be concluded that only the Lagrange scenario could describe the cold α ternary fission of ^{252}Cf. The paper is organized as follows: a semiclassical approach to the tunneling problem in many body systems is examined in Sec. II, the main characteristics of a three body potential appropiate for α ternary fission are discussed in Sec. III, Sec. IV discusses selected α particle trajectories and ternary barriers, the results for α particle ternary yields are shown in Sec. V, a brief comparison of the calculated yields with the experimental ones is presented in Sec. VI and some conclusions are drawn in Sec. VII.

II. TUNNELING IN MANY BODY SYSTEMS

The penetration problem for multidimensional barriers has been studied by many authors [18–23] mainly in connection with the enhancement of fusion cross sections in sub-Coulomb heavy ion reactions. In this section we describe a semiclassical approach to the tunneling process in a many body system. The system consists of n bodies interacting via a potential $V(\{q_i\})$ which is the sum of two body components. This assumption is not very restrictive and may be relaxed. $\{q_i\}$ is a set of N generalized coordinates. The total available energy of the system is identified with the decay energy Q. In the classically forbidden region ($V \gg Q$) the usual WKB conditions are assumed to be fulfilled and the semiclassical many body wave function is given by

$$\Psi \propto \exp(-S_0/\hbar), \tag{1}$$

where S_0 is the reduced action between the entrance point (to be specified later) and the current point [21,24]. The wave function (1) is also proportional to a preexponential factor which includes the quantum characteristics of the molecular state prior to penetration and high order corrections of the WKB approximation. The exponential factor is the most important one since it varies faster than the preexponential one [21] ($S_0/\hbar$ takes values of the order of a few tens).

The action satisfies the Hamilton-Jacobi equations. Consequently the equations of motion (in imaginary time) are the (modified) Euler-Lagrange equations and the trajectory satisfies the Maupertuis principle [25]. For the Lagrangian

$$\mathcal{L} = \frac{1}{2} \sum_{i,j=1}^{N} a_{ij} \dot{q}_i \dot{q}_j - V(\{q\}), \tag{2}$$

the reduced action may be written as

$$S_0 = \int \sqrt{2(V-Q)\sum a_{ij} dq_i dq_j} \tag{3}$$

and the trajectory is obtained by extremizing S_0 with respect to all possible paths in the coordinates q_i. Parametrizing the path by one of the coordinates, say, q_1, a set of coupled equations is obtained:

$$\frac{\partial V}{\partial q_i} = \frac{1}{M} b_i \left(V' + \sum_k \frac{\partial V}{\partial q_k} q_k' \right) + \frac{2}{M}(Q-V)$$
$$\times \left[\frac{1}{M} b_i \left(\sum_k a_{1k} q_k'' + \sum_{kl} a_{kl} q_k' q_l'' \right) - \sum_k a_{ik} q_k'' \right], \tag{4}$$

where $i,k,l = 2/N$ and $f' = \partial f/\partial q_1$. The quantity b_i is defined by

$$b_i = a_{1i} + \sum_k a_{ik} q_k'$$

and the effective mass of the system by

$$M = a_{11} + 2\sum_i a_{1i} q_i' + \sum_{ik} a_{ik} q_i' q_k'. \tag{5}$$

To the first order of the WKB approximation, the penetrability is given by the square of the wave function (1) with the reduced action calculated on the path satisfying Eq. (4) and the boundary conditions

$$V(\{q_i^{in,out}\}) = Q. \tag{6}$$

In the particular case $N=1$ this condition uniquely determines the penetration path. In the general case, the condition (6) does not specify all the necessary conditions for integrating Eq. (4). In principle we should solve Eq. (4) for all solutions satisfying Eq. (6) and choose the path $q_i(q_1)$ which minimizes the reduced action not only with respect to such paths but also to the entrance points [21]:

$$S_0 = \int_{in}^{out} \sqrt{2M(V-Q)} dq_1, \tag{7}$$

where

$$M = M(q_i(q_1), q_1), \quad V = V(q_i(q_1), q_1). \tag{8}$$

The evaluation of the WKB penetrability does not involve any fluctuation in the entrance point since this is uniquely defined by the condition that the action be lowest with respect to it. Such fluctuations would be important for an evaluation of a complete result such as an energy and angular distribution for the fragments and are mainly entering in the preexponential factor in Eq. (1). However , such corrections are presumably the same for different fragmentations and drop out in the relative yield calculatations we are interested in this paper. As is well known the WKB approximation is not valid near the turning points. Nevertheless, we extend its validity even in such regions since this procedure is not expected to bring in important errors in most realistic calculations.

In the particular case of a diagonal mass tensor $a_{ik} = \mu_i \delta_{ik}$, Eq. (4) gets a much simpler form:

$$M \frac{\partial V}{\partial q_i} = \mu_i q_i' \left(V' + \sum_k \frac{\partial V}{\partial q_k} q_k' \right) + 2\mu_i (Q-V)$$

$$\times \left(\frac{q_i'}{M} \sum_k \mu_k q_k' q_k'' - q_i'' \right) \tag{9}$$

and the effective mass reduces to

$$M = \mu_1 + \sum_k \mu_k (q_k')^2. \tag{10}$$

Let us stress that the system of equations (6)–(10) does not represent a trivial generalization of the tunneling problem in one dimension. The main difference stems from the fact that Eq. (6) has in general many solutions and the integration of the highly nonlinear coupled equations (9) cannot be started without imposing additional constraints on physical trajectories.

To fix the ideas, let us discuss in some detail the specific features of the tunneling process in the case of cold α accompanied ternary fission. We assume that all three fragments are preexisting in a quasibound molecular state. Since the process is cold, the heavy fragments have very compact shapes with deformations close to their asymptotic values. Strong polarization effects are expected in the initial stages

of the tunneling process. One may include such effects by introducing effective deformations. In order to grasp the penetrabilities for the most probable processes one may consider only axial deformations with the symmetry axis oriented along the fission axis. For simplicity the problem is reduced to a planar one and therefore we have to deal with six coordinates. Requiring the c.m. to be at rest, we are left with four independent coordinates. Let $(x_i, y_i, i=1,2)$ be the fragment coordinates and (x_α, y_α) the coordinates for the α particle. The corresponding masses are denoted by $m_i, i=1,2,\alpha$. The usual transformation to relative coordinates $R = x_2 - x_1$ and $y = y_2 - y_1$ leads to

$$x_1 = \frac{-m_\alpha x_\alpha - m_2 R}{m_1 + m_2}, \quad y_1 = \frac{-m_\alpha y_\alpha - m_2 y}{m_1 + m_2},$$

$$x_2 = \frac{-m_\alpha x_\alpha + m_1 R}{m_1 + m_2}, \quad y_2 = \frac{-m_\alpha y_\alpha + m_1 y}{m_1 + m_2}.$$

The kinetic energy and the third component of the angular momentum in terms of these coordinates are

$$T = \frac{1}{2} [\mu_{12}(\dot{R}^2 + \dot{y}^2) + \mu_\alpha (\dot{x}_\alpha^2 + \dot{y}_\alpha^2)], \tag{11}$$

$$L_z = \mu_{12}(R\dot{y} - \dot{R}y) + \mu_\alpha (x_\alpha \dot{y}_\alpha - \dot{x}_\alpha y_\alpha), \tag{12}$$

where

$$\mu_{12} = \frac{m_1 m_2}{m_1 + m_2}, \quad \mu_\alpha = m_\alpha \left(1 + \frac{m_\alpha}{m_1 + m_2} \right).$$

Since the α particle mass is small compared to the fragment masses, we further assume $y \approx 0$ on the penetration path. This assumption may lead to a nonconservation of the angular momentum (12). However, we expect a very smooth α particle trajectory, and to a good approximation the second term in Eq. (12) is vanishingly small. Next, requiring $L_z = 0$ implies $y \simeq \text{const} \times R$. In the initial configuration one can always choose the heavy fragments along the x axis and therefore const=0 and the angular momentum is approximately conserved. Similar considerations lead to the conclusion that even the kinetic energy (11) is well evaluated along the trajectory. Since $y \approx 0$ seems to be a reasonable approximation, one further assumes $y_1 \approx y_2 \approx 0$.

We are finally left with the problem of finding the α particle coordinates (x_α, y_α) as a function of the interfragment distance R, which is a natural candidate for the variable q_1. A close inspection of Eq. (11) readily identifies the necessary mass parameters and the action integral reads

$$S_0 = \int_{R_{in}}^{R_{out}} \sqrt{2 \left\{ \mu_{12} + \mu_\alpha \left[\left(\frac{\partial x_\alpha}{\partial R} \right)^2 + \left(\frac{\partial y_\alpha}{\partial R} \right)^2 \right] \right\} (V-Q)} \, dR, \tag{13}$$

with $V = V(x_\alpha(R), y_\alpha(R), R)$. The above formula shows that under well-justified approximations the penetrability for the three body system is similar to the well-known WKB expression for two body systems with an important correction in

the effective mass arising from the α particle trajectory. The one dimensional case is exactly recovered in the limit $m_\alpha \rightarrow 0$. The magnitude of the correction can be determined by solving the nonlinear coupled equations (9). Subsequent numerical calculations with selected trajectories showed that the most important corrections arise from the variation of y_α with the interfragment distance and the presence of α fragment components in the potential.

III. THREE BODY POTENTIAL

As already mentioned, the three body potential is computed with the help of the double folding potential generated by the M3Y-NN effective interaction and realistic deformations (see details in Ref. [3]). The total interaction potential is obtained as the sum of two body potentials between the α particle and the fragments and between the light and heavy fragments. An advantage of this approach is that the barrier between the two fragments and the barrier between the α particle and the fragments can be calculated quite accurately due to the fact that the touching configurations are situated outside the barriers. However, we must recognize that there are a few shortcomings in using the M3Y interaction for generating heavy ion potentials appropiate for fission calculations. The M3Y effective interaction, which is typical for the so called G-matrix density independent interactions (see [27] for a recent review), is dominated by the exchange component in each spin-isospin (S,T) channel. In the heavy ion case, these components lead to a complicated nonlocal potential. However, the range of nonlocality is rather small due to the large masses involved and in the standard version of the model the nonlocal potential is replaced by a local equivalent potential generated by a pseudo-δ interaction with a strength depending slightly on energy. The lack of any density dependence leads to unphysically deep potentials for large density overlaps. Such deep potentials can hardly accomodate the molecular picture. One way to correct the short range dependence of the interaction potentials is to introduce a repulsive component in the effective interaction with a strength adjusted to fit the result obtained with proximity forces [31] or to use the Yukawa-plus-exponetial form of the liquid drop formula of Möller and Nix [17]. However, throughout this paper, the penetration path starts always at distances beyond the touching configurations and for well separated nuclei, the M3Y interaction produces realistic potentials. This feature prevailed since we believe it to be extremely important to work with correct barriers on the absolute energetic scale. The error in treating the short range part of the interaction potentials does not influence in a significant way our results. One should stress that approximating the many body interaction potential by a sum of two body components is only justified for small density overlaps. We stress again that all penetrability calculations involve density overlaps significantly less than the nuclear matter saturation density. This point was checked carefully in all calculations.

The database for the present calculation includes 78 different splittings for α ternary fission and 87 splittings for binary fission of ^{248}Cm. Each splitting is defined by charge and mass numbers, experimental binary and ternary decay

energies, and a set of geometrical and deformation parameters which characterize the one body densities. Such a large scale calculation requires accurate techniques for evaluating the six dimensional integrals entering the folding model [27,28]:

$$V(\vec{R}) = \int d\vec{r}_1 d\vec{r}_2 \rho_1(\vec{r}_1) \rho_2(\vec{r}_2) v(|\vec{s}|), \qquad (14)$$

where $\rho_{1,2}(\vec{r})$ are the ground state one body densities of the fragments (not necessarily spherical) and v is the NN effective interaction. The separation distance between two interacting nucleons is denoted by $\vec{s} = \vec{r}_1 + \vec{R} - \vec{r}_2$, where $\vec{R}$ is the distance between the centers of mass of the two fragments. A harmonic oscillator density with a width parameter $\beta^2 = 0.47$ fm^{-2} was used for the α particle. For the heavy fragments, the one body densities are taken as Fermi distributions in the intrinsic frame:

$$\rho(\vec{r}) = \rho_0 \left[1 + \exp\left(\frac{r-C}{a}\right) \right]^{-1}, \qquad (15)$$

with $C = C_0[1 + \Sigma_{\lambda \geq 2} \beta_\lambda Y_{\lambda 0}(\Omega)]$. Only static axial symmetric deformations are considered. The half radius C_0 and the diffusivity are taken from the liquid drop model [17]. The volume conservation is ensured by requiring normalization to the particle number

$$\int r^2 dr d\Omega \rho(r,\Omega) = A, \qquad (16)$$

and the density multipoles are computed numerically:

$$\rho_\lambda(r) = \int d\Omega \rho(r,\Omega) Y_{\lambda 0}(\Omega). \qquad (17)$$

Using the multipole expansion of the densities, the integral in Eq. (14) becomes

$$V(\vec{R},\omega_1,\omega_2) = \sum_{\lambda_1 \mu_1 \lambda_2 \mu_2} D^{\lambda_1}_{\mu_1 0}(\omega_1) D^{\lambda_2}_{\mu_2 0}(\omega_2) I_{\lambda_1 \mu_1 \lambda_2 \mu_2}(R), \qquad (18)$$

where [28]

$$I_{\lambda_1 \mu_1 \lambda_2 \mu_2}(R) = \sum_{\lambda_3 \mu_3} B^{\lambda_3 \mu_3}_{\lambda_1 \mu_1 \lambda_2 \mu_2} Y_{\lambda_3 \mu_3}(\hat{R})$$

$$\times \int r_1^2 dr_1 dr_2^2 r_2 \rho_{\lambda_1}(r_1) \rho_{\lambda_2}(r_2)$$

$$\times F^v_{\lambda_1 \lambda_2 \lambda_3}(r_1, r_2, R) \qquad (19)$$

and

$$F^v_{\lambda_1 \lambda_2 \lambda_3}(r_1, r_2, R) = \int q^2 dq \, \tilde{v}(q) j_{\lambda_1}(qr_1) j_{\lambda_2}(qr_2) j_{\lambda_3}(qR). \qquad (20)$$

Above, $D^\lambda_{\mu 0}(\omega)$ stands for the Wigner rotation matrix describing the orientation ω of the intrinsic symmetry axis with
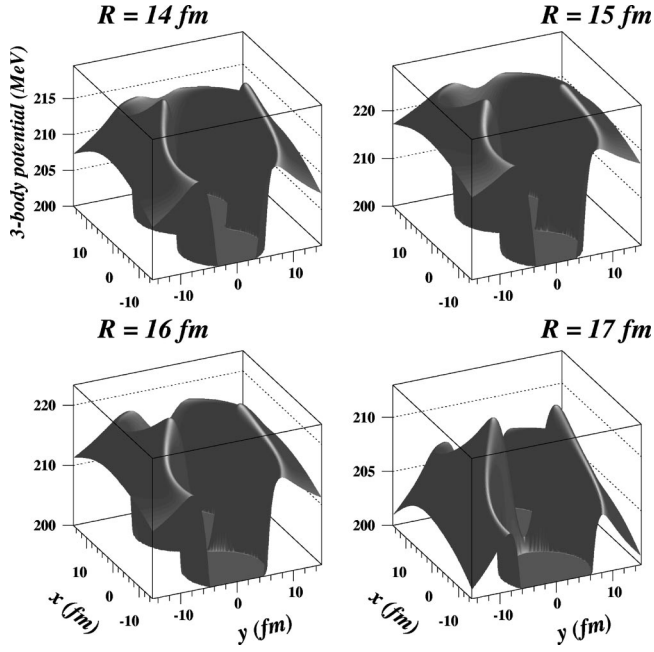
FIG. 1. The three-dimensional ternary potentials for the splitting $^4\text{He}+{}^{92}\text{Kr}+{}^{156}\text{Nd}$ at different interfragment distances $R=14$, 15, 16, 17 fm between the collinear fragments in a nose to nose configuration. We can see the two wells corresponding to the light and heavy fragments and in the equatorial plane a ridge which grows up with the interfragment distance R. This ridge has a minimum on the symmetry axis and a maximum at the equatorial α barrier height. This minimum disappears at large interfragment distances $R \simeq 20$–21 fm.

FIG. 3. The ternary potentials $V(x_\alpha, y_\alpha = 0, R)$ for the splitting $^4\text{He}+{}^{92}\text{Kr}+{}^{156}\text{Nd}$ as a function of x_α for different interfragment distances R. The two wells and the two polar barriers corresponding to the light and heavy fragments are clearly seen. At $R>17$ fm the polar barriers are below the ternary Q_3 value. The interfragment ridge situated in the equatorial plane is very narrow.
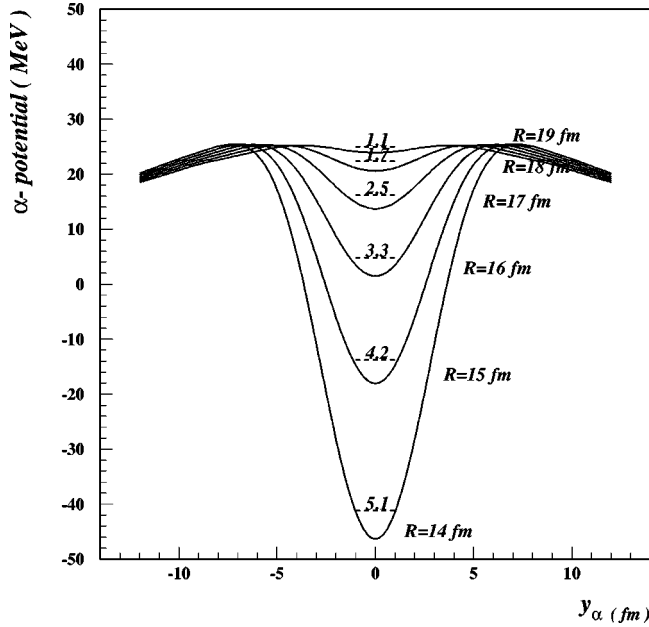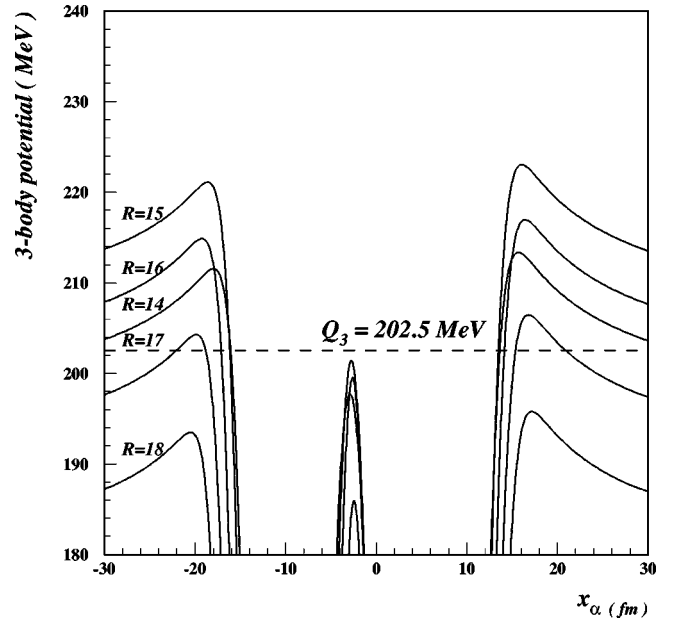

FIG. 2. The ternary potential minimum in the equatorial plane for the splitting $^4\text{He}+{}^{92}\text{Kr}+{}^{156}\text{Nd}$ at different interfragment distances R. The corresponding zero point energies in a harmonic oscillator approximation are indicated. As can be seen at large R this minimum disappears.

respect to the fixed frame, $\tilde{v}(q)$ denotes the Fourier transform of the interaction, and j_λ are spherical Bessel functions. The matrix B [28] contains selection rules for coupling angular momenta. For example, only even $\lambda_1 + \lambda_2 + \lambda_3$ are allowed. If both fragments have nonvanishing deformations up to $\lambda_{1,2} = 4$, then the sum in Eq. (18) involves 32 incoherent terms for a nose-to-nose configuration and total angular momentum restricted to $\lambda_3 \leq 6$. For translationally invariant one body densities, the interaction potential in Eq. (14) is also translationally invariant. Since the simple Fermi distributions does not satisfy this requirement, the folding integral contains a spurious dipole c.m. contribution which is disregarded in Eq. (18).

Numerical techniques for evaluating the highly oscillating integrals appearing in Eq. (20) are described in detail in [28] and will not be repeated here. Extensive numerical calculations [3,16] have shown that the magnitude and particularly the sign of the deformation parameters have a dramatic influence on the calculated potentials in the barrier region. At the scission configuration we have assumed prolate shapes for the heavy fragments in contact at their tips. Prolate shapes lead to much lower barriers and are favored in fission. For *pear* shapes, i.e., fragments with quadrupole and octupole deformations, we choose opposite signs for the octupole deformations of the two fragments. It is easy to show that the transformation $\beta_3 \rightarrow -\beta_3$ leads to a simple rotation with $\theta = \pi$ and therefore does not change the nuclear shape. The sign question of the hexadecapole deformation is much more delicate. To avoid complications, we have systematically chosen the absolute value for this parameter, and thus overestimated to some extent the corresponding penetrabilities.

In order to understand the landscape of the three body potential we first represent the potential at different interfragment distances R (Fig. 1) with heavy fragments in a nose to nose configuration, for the splitting ^{4}He$+^{92}$Kr$+^{156}$Nd with deformed fragments. The potential for a splitting with a spherical fragment looks quite similar. In the equatorial plane we distinguish a saddle configuration which results from the interplay of the strong repulsive (Coulomb) forces acting on the α particle and the attractive (nuclear) forces. The saddle trajectory is obtained by numerically solving the equation

$$\frac{\partial V}{\partial x_\alpha} = 0$$

for fixed interfragment distance. Along the saddle trajectory there are two interesting extrema: one is situated on the symmetry axis and another one at the top of the maximum of the equatorial α barrier ridge where all classical forces acting on the α particle are equilibrated. This last point is denoted in the following as the Lagrange point and the ensemble of such points for different interfragment distances as the Lagrange trajectory. As can be seen in Fig. 1 the minimum situated on the symmetry axis disappears at large interfragment distances $R = 20-21$ fm. Following Radi *et al.* [29], we assume that the position of the α particle is governed by the well the potential has in the perpendicular direction. If the motion is not very fast, the α particle should adiabatically adjust to a stationary state in this potential. To get the position of the α particle we approximate this potential with a harmonic oscillator potential:

$$V(y) = V_{\min} + \frac{1}{2} C y^2, \tag{21}$$

where the stiffness coefficient C depends on the interfragment distance and is obtained by numerically differentiating the potential around the minimum. Then the eigenvalues are given by

$$E_n = \left(n + \frac{1}{2}\right) \hbar \sqrt{C/m_\alpha}. \tag{22}$$

A convenient measure of the spread of the position is given by

$$\langle y^2 \rangle_n = E_n/C. \tag{23}$$

In Fig. 2 the saddle potential and the zero point energies are represented as a function of R for the splitting ^{4}He$+^{92}$Kr$+^{156}$Nd with deformed fragments. The zero point energies are consistent with the previous estimation of Radi *et al.* [29]. In Fig. 3 we represented the polar α barriers, i.e., the potential $V(x_\alpha, y_\alpha = 0, R)$ for the same splitting and at different interfragment distances R. The two wells corresponding to the light and heavy fragments which are separated by a very narrow interfragment ridge can be clearly seen. The polar barriers disappear at the interfragment distance $R \simeq 17$ fm, which is much earlier than the equatorial barriers. We must stress that the semiclassical approximation
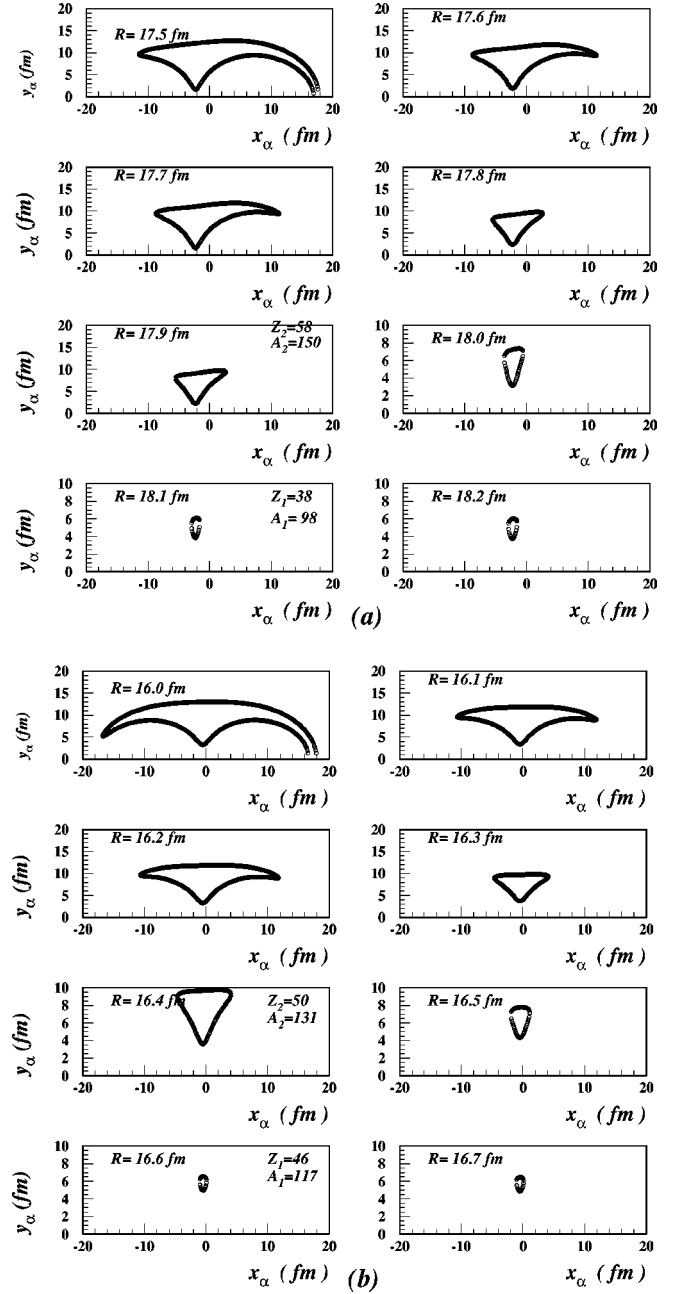

FIG. 4. The ternary potentials $V(x_\alpha, y_\alpha, R)$ represented in the plane (x_α, y_α) by the single equipotential line $V = Q_3$ at different interfragment distances R for the splittings: (a) ^{4}He$+^{92}$Kr$+^{156}$Nd with deformed fragments and (b) ^{4}He$+^{117}$Pd$+^{131}$Sn with a spherical heavy fragment. At large R the exit points are quite different for such splittings. This suggests different energy and angular distributions of the α particle for the two regions.

for the penetration factor requires the penetration path to be localized in a region where $V \geq Q$ where V is the total interaction energy and Q is the decay energy. This is the most economic way to localize the position of the α particle along the penetration path in the present model. In Figs. 4(a) and 4(b), for the above splitting with deformed fragments and the splitting ^{4}He$+^{117}$Pd$+^{131}$Sn with a spherical fragment, we represented the three body potential $V(x_\alpha, y_\alpha, R)$ in the
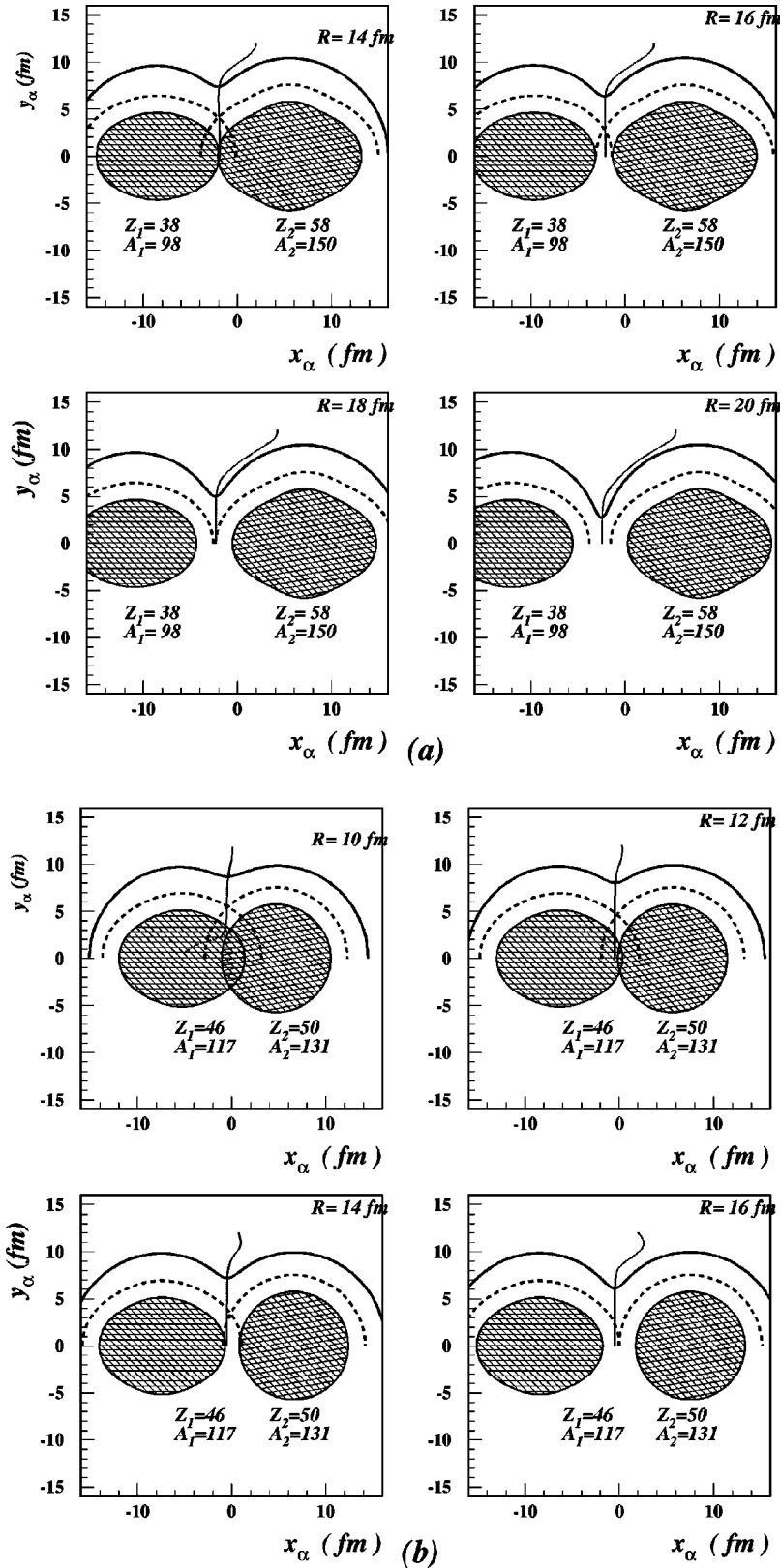
FIG. 5. Schematic representation of the two fragments for the splittings (a) and (b) mentioned in Fig. 4. The fragment shape is defined by the the half-density surface. The dashed line represents the locus of the center of the α particle in touching with one of the fragments. The thick solid line represents the α particle ridge while the thin line is the equatorial ridge. The intersection of the two solid lines gives the Lagrange point (see the text for details).

plane (x_α, y_α) at different interfragment distances by only one equipotential line $V = Q$. At small interfragment distances the uncertainty in the α particle position is rather large but it reduces drastically as R increases. It may be seen that by increasing R the Q-value contours are reduced practically to a single point. One remarks also that at the exit points the y coordinate of the α particle is rather large with values of the order of 5 fm for two deformed fragments and slightly larger (6 fm) when one fragment is spherical. Such high values are consistent with Eq. (23) only if the α particle is

placed in a rather high excited state in the saddle potential. Also one can remark that the penetration path ends earlier in the case of one spherical fragment as compared to the deformed-deformed case. Based on this observation one may conjecture that the angular and energy distributions of the α particle which are largely determined by the configuration at the end of the penetration path will be rather different in the two cases.

Other possible characteristics of the three body potential are given in Figs. 5(a) and 5(b). Here we represented in the plane (x_α, y_α) for the above two splittings the fragments with all deformations included and the two ridges: the equatorial one defined by the equilibrium of the classical forces acting on the α particle in the x direction and the α particle ridge defined by the top of the α barriers situated around the two fragments. The intersection of these two ridges gives the Lagrange point where no net forces are acting on the α particle. The centers of the α particle obtained from the geometrical condition that the α particle be in touch with each fragment are also represented. A touching point is defined such that the densities of the two bodies in contact in that point are half of their central value. As a rule the intersection of the two touching configurations of the α particle and the two fragments is not situated on the equatorial ridge. Because of the fact that this ridge is very narrow (see Fig. 3), we have to impose the condition that the α particle be in equilibrium on the ridge, in order to exclude the cases of subsequent disolution of the α particle in one of the fragments. This condition together with the touching condition with one of the fragments defines the adiabatic trajectory when the interfragment distance is varied. It is worth mentioning that the strong density overlap especially in Fig. 5(b) has only an illustrative purpose to show how the trajectories defined above evolve with the interfragment distance and in that such configurations are never involved in the calculations. We recall here that the Lagrange trajectory which explores the maximal values of the interaction potential gives a lower bound of the penetrability while the more physically intuitive adiabatic trajectory gives an upper bound.

One possible physical choice of the α particle initial position is situated on the interfragment ridge and above the touching curves as previously defined. On the other hand, different scenarios related to the excited quantum states defined in the equatorial ridge well can be considered.

IV. α PARTICLE TRAJECTORIES AND TERNARY BARRIERS

In our static description of the α accompanied fission, the α ternary yields depend essentially on the α particle trajectory. The numerical integration of the trajectory (9), is a difficult task for the large number of fragmentations necessary for relative yield calculations. In the following we content ourselves to consider a number of physically reasonable trajectories intended to give an idea of the penetration probability in a three body system.

The *first* one is the *adiabatic scenario*. This assumes that the α particle is situated on the interfragment ridge, satisfying one of the two touching configurations, i.e., at the lowest
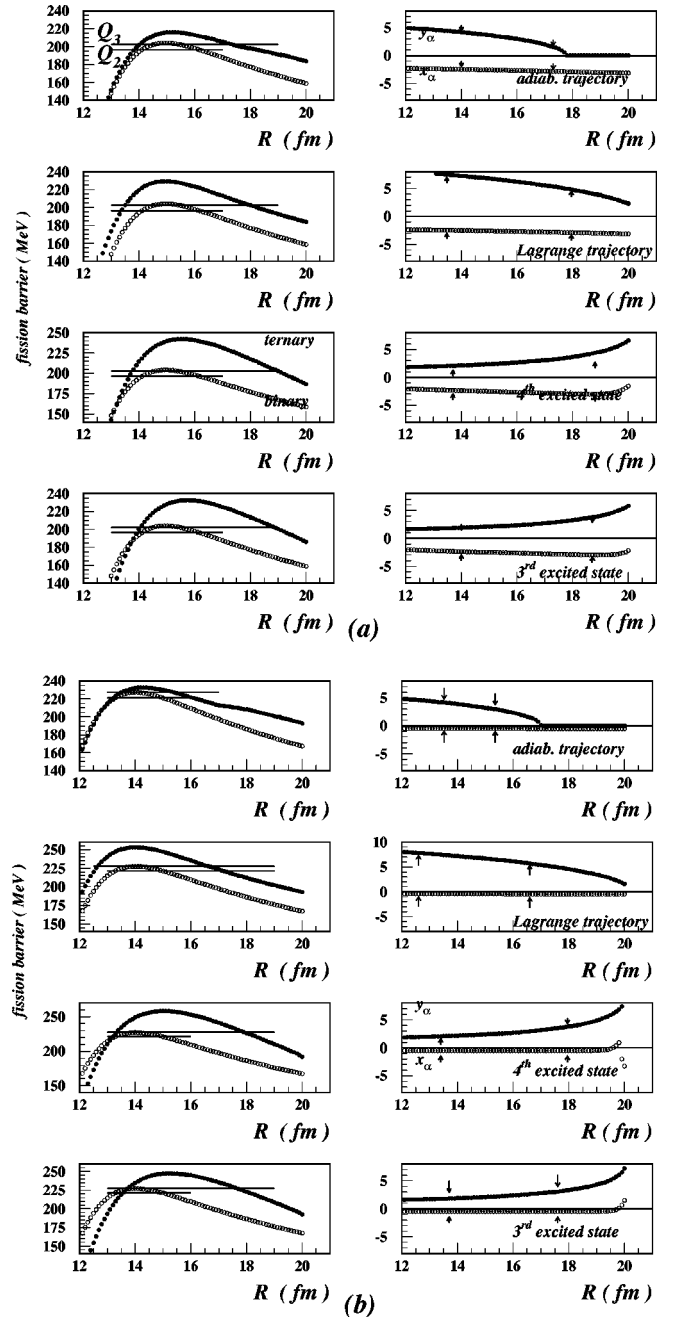

FIG. 6. Fission barriers and α particle trajectories for the splittings (a) and (b) mentioned in Fig. 4. Left panels: ternary barriers calculated along selected trajectories and binary barriers for the cold fission of the daughter nucleus ^{248}Cm leading to the same fragments. The corresponding ternary and binary reaction energies are indicated by thin lines. Right panels: the α particle trajectories (x_α, y_α versus the interfragment distance R). The inner and outer turning points are indicated by arrows.

initial y_α value. By increasing the interfragment distance R, the α particle is getting closer to the fragment symmetry axis. The corresponding α particle trajectory together with the ternary and binary barriers is plotted in Figs. 6(a) and 6(b) for the above two splittings: (a) ^{4}He$+^{92}$Kr$+^{156}$Nd and (b) ^{4}He$+^{117}$Pd$+^{131}$Sn. Also represented is the intersection

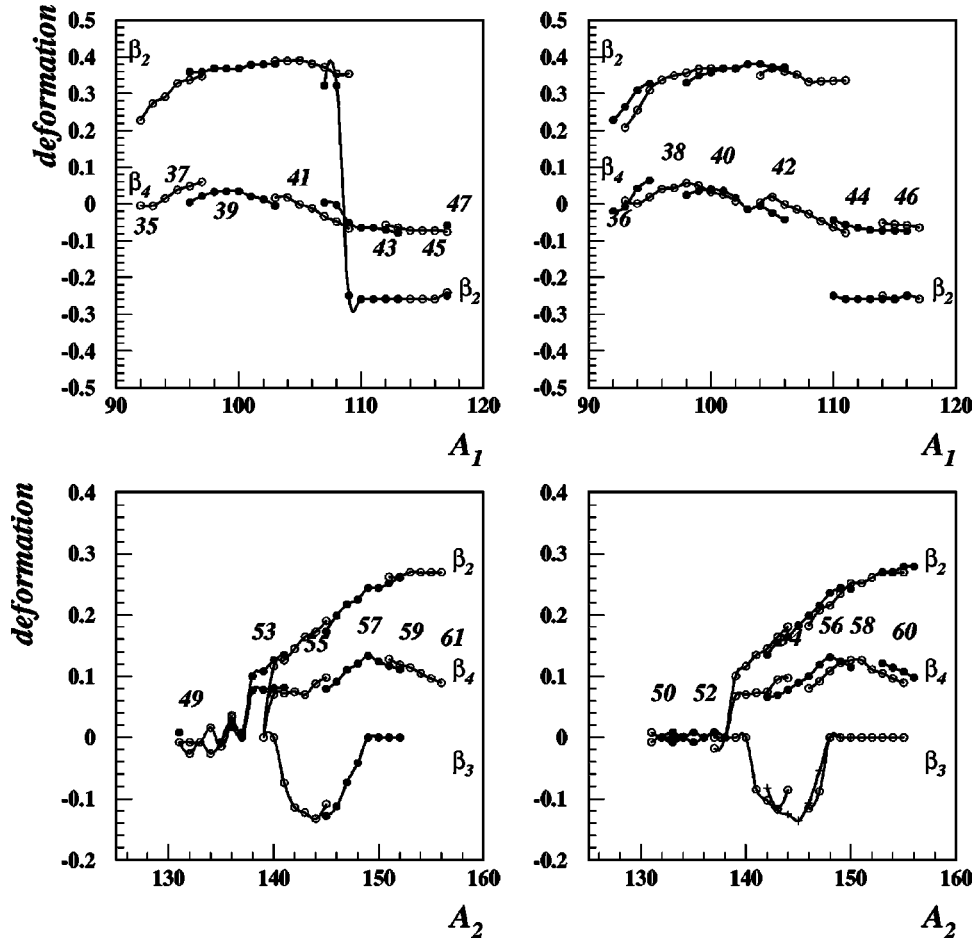FIG. 7. The assumed β_λ ($\lambda = 2,3,4$) ground state deformations taken from Ref. [17]. Note that light fragments (Z_1, A_1) have mainly quadrupole deformations in contrast to heavy fragments (Z_2, A_2) which can have all kinds of deformations. The octupole deformations are present in a small region $141 \leqslant A_2 \leqslant 148$ whereas the hexadecupole deformations are important in the region $138 \leqslant A_2 \leqslant 158$. The fragments with $A_1 \leqslant 94$ and $A_2 \leqslant 138$ are practically spherical.

of the barriers with the Q values, giving the corresponding inner and outer turning points. Note that the system crosses the ternary barrier before the α particle becomes collinear with the fragments.

The *second* scenario is the *Lagrange scenario*. In this case the α particle is situated at the Lagrange point were all forces acting on the α particle are in equilibrium. The α particle trajectories and the corresponding barriers are represented also in Figs. 6(a) and 6(b). The binary barriers of ^{248}Cm for the same splittings are also plotted. Clearly the ternary barrier is higher than the binary one and shifted to larger R distances. As previously discussed the α particle motion in the transversal well is taken into account by substracting from the Q_3 value its energy (22). This procedure does not provide for a ternary barrier above the Q_3 value when considering the ground and first excited states. Therefore we consider only the third and fourth excited state *scenarios*. In the same Figs. 6(a) and 6(b) the α particle trajectories and the corresponding ternary barriers for the third and fourth excited states are represented by including the $E_n(R)$ values in the barriers. Obviously, for these scenarios the y_α initial values of Eq. (23) are smaller than for the Lagrange configuration, which assumes the maximum y_α values at the top of the α barriers, and even smaller than the values for the adiabatic scenario which is based on the lowest energy configuration.

V. α PARTICLE TERNARY YIELDS

Knowing the barriers and Q_3 values, the relative α ternary yields are given as ratios of the penetrability for a given splitting $P(A_L, Z_L)$ calculated with Eqs. (1) and (13) and the sum of penetrabilities for all possible splittings:

$$Y_L(A_L, Z_L) = \frac{P(A_L, Z_L)}{\Sigma_{L'} P(A_{L'}, Z_{L'})}. \tag{24}$$

It is known that the preformation factors for an α particle at the surface of a deformed fragment differs by orders of magnitude as compared to the spherical case. Nevertheless, in this paper no preformation factors are considered; i.e., it is assumed that the preformation factors are the same for all cold splittings and consequently in the expression (24) of the relative yields this factor cancels. For the fragment deformations we choose the ground state deformations of Möller *et al.* [17] computed in the framework of the macroscopic-microscopic model. These deformations play a very important role in barrier penetrabilities, i.e., in ternary yields. In Fig. 7 we represented these deformations for the light and heavy fragments separately for odd and even charges Z. Note that the light fragments have mainly quadrupole deformations in contrast to heavy fragments which have all kinds of deformations. The octupole deformations exist for a small
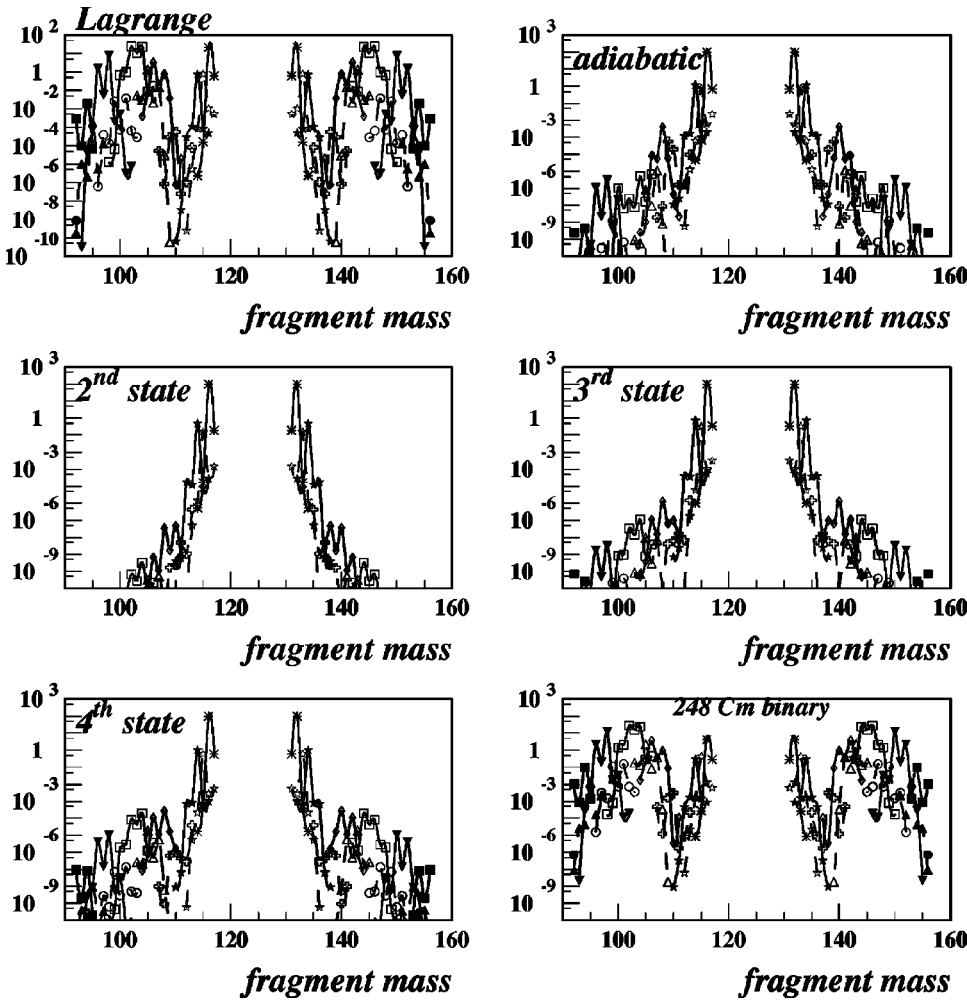
FIG. 8. The cold α ternary yields of ^{252}Cf for the Lagrange, adiabatic, second, third, and fourth state scenarios, corresponding to different initial positions of the α particle on the interfragment ridge, as a function of the fragment mass. The list of symbols is displayed in the upper left panel of Fig. 9. Also the cold binary fission yields of ^{248}Cm are given. With the exception of ternary yields obtained in the Lagrange scenario, which are very similar with the cold binary yields of ^{248}Cm, all scenarios strongly favor the splitting ^{4}He+^{116}Pd +^{132}Sn with one spherical fragment.

heavy fragment mass region $141 \leq A_H \leq 148$. The fragments with mass numbers $A_L < 92$ and $A_H < 138$ are practically spherical. In the following we include all deformations up to $\lambda = 4$ with positive values; i.e., oblate shapes ($\beta_2 < 0$) are transformed to prolate shapes ($\beta_2 > 0$) and neck shapes ($\beta_4 < 0$) to shapes with positive hexadecapole deformations ($\beta_4 > 0$). This figure suggests that cold fission yields in the region $92 \leq A_L \leq 108$ and $140 \leq A_H \leq 156$ with deformed fragments and also in the region around ^{132}Sn with at least one spherical fragment are to be expected. The Q values are calculated from experimental mass tables [26] but for some splittings the nuclear masses from the microscopic-macroscopic model of Möller *et al.* [17] are used.

The ternary fission yields for different scenarios—Lagrange, adiabatic, second, third, and fourth excited states—corresponding to different initial positions of the α particle on the interfragment ridge are represented in Fig. 8. Also the cold binary yields for ^{248}Cm are given. With the exception of the Lagrange scenario yields, which are very similar to the cold binary yields of ^{248}Cm, all other scenarios are strongly favoring only the spherical splittings.

In Fig. 9, for the same scenarios, the ternary yields versus binary yields of the daughter nucleus ^{248}Cm leading to the same splittings are displayed. Only in the Lagrange scenario are the α ternary yields strongly correlated with the cold

binary yields of the daughter nucleus. Such a possibility is consistent with the fact that binary barriers are very thin (widths of the order of 2–3 fm) [16]. For the other scenarios—adiabatic, second, third, and fourth excited states—only the ternary yields for spherical splittings, which are dominated by the Q-value principle become important. This fact is not consistent with the existing experimental data on cold α ternary yields [14], which indicate cold α ternary yields for both regions.

VI. COMPARISON OF EXPERIMENT AND THEORY

Neutronless α ternary fission yields were observed experimentally in the spontaneous fission of ^{252}Cf [14]. They are displayed in Fig. 10 together with the theoretical yields calculated in the *Lagrange* scenario. The theoretical yields are normalized to the total experimental yield. The highest experimental yields are found for the Zr+Ba isotopes, a feature which is reproduced correctly by the model. Significant yields were also found for the Mo+Xe and Sr+Ce ternary fragmentation, too. We point out that all the neutronless α ternary even-Z fragmentations of ^{252}Cf which have relative isotopic yields larger than 0.02% and whose fragments have known low energy gamma transitions were experimentally identified. Of course, other fragmentations corresponding to
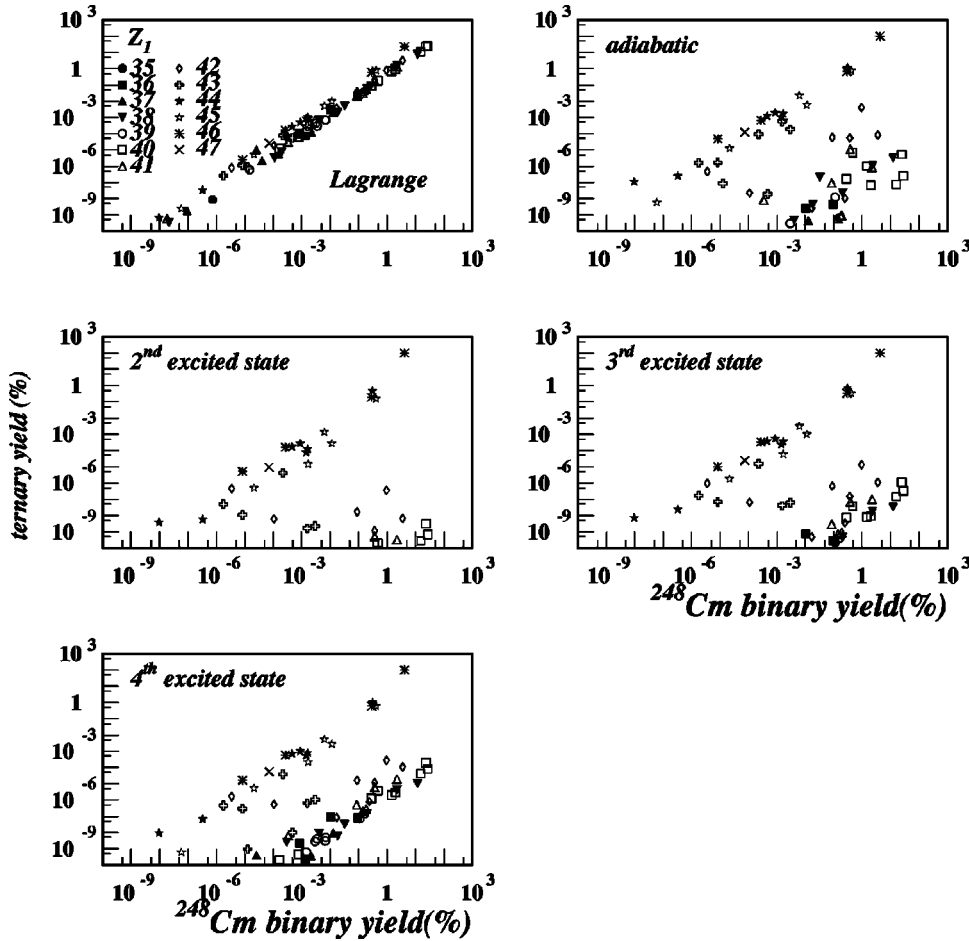
FIG. 9. Scatter diagram of the cold α ternary yields of ^{252}Cf for Lagrange, adiabatic, second, third and fourth excited state scenarios versus the cold binary yields of ^{248}Cm. Only the ternary yields of ^{252}Cf obtained in the Lagrange scenario are strongly correlated with the cold binary yields of the daughter nucleus ^{248}Cm. For all other possible scenarios only the splitting with ^{132}Sn is favored.

a lighter fragment ^{105,106}Zr, ^{109,110}Mo, and ^{114}Ru should be observed and plenty of odd-Z fragmentations must be observed too, though the latter are much more difficult from an experimental point of view due to the huge structure of the low energy γ spectra.

Enhanced experimental yields were found for cold α ternary fission in which the heavier partners are Ba isotopes with masses ranging from 144 to 148. Their higher yields are due to the static octupole deformations observed in this region (see Fig. 7), since octupole shapes at the scission configuration significantly lower the Coulomb barrier and increase the penetrability between the final fragments. Similar enhanced yields have already been detected in the cold binary fission of ^{252}Cf [10].

A few of the cold fragmentations presented in Fig. 10 involve odd-odd splittings, and one can observe that their corresponding experimental yields are comparable or even larger than the yields for the even-even neighbors. The calculated yields do not include differences in the level densities near the ground state of the even-even and odd-odd nuclei. Consequently, these yields for the odd-odd splittings are underestimated. The same yields for the double-magic nucleus ^{132}Sn (light partner ^{116}Pd) and its neighbors result in too high values, because of the lower level densities in this region. Also the experimental yield for the ^{132}Sn could be underestimated due to the fact that with the Gammasphere one cannot detect yields going directly to the ground state of

one or both fragments. In that particular case only transitions above the the first excited state at 4.04 MeV were considered for the integrated yields.

We want to emphasize that the experimentally determined isotopic yields are integrated yields. In the spontaneous fission experiment of ^{252}Cf the majority of binary and ternary splittings lead to highly excited final nuclei, which after neutron evaporation are decaying to the lowest states by γ cascades. Less frequently, there are also cold fragmentations which leave the final nuclei in their ground or first excited state. These cold fission experimental yields were defined [14,30] as integrated yields since they collect the contributions of all neutronless fragmentations over a whole range of TXE's from zero up to at least the neutron binding energy, from where the evaporation of a first neutron becomes possible. The theoretical yields calculated with slightly adjusted (of the order of a few percent) quadrupole deformations parameters should not be compared directly with the experimental yields since the former ones correspond only to transitions to the ground states of the final nuclei. Thus Fig. 10 has only an illustrative purpose. Nevertheless, one can see from the figure that the model has a relatively good predictive power; for most of the observed splittings the theoretical yields are in the right order of magnitude.

VII. CONCLUSIONS

In the present paper, based on a three body cluster model, we studied the α ternary cold (neutronless) fragmentations of
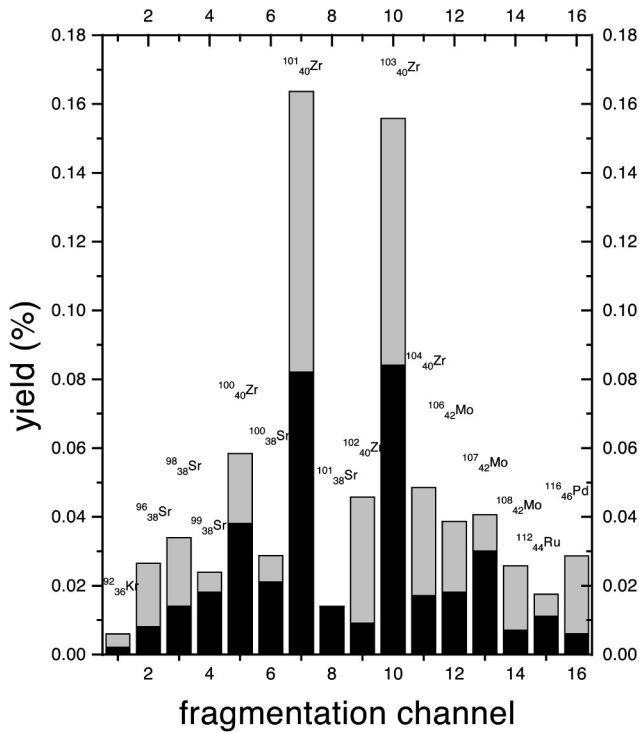
FIG. 10. Diagram presenting the experimentally determined α ternary cold fission yields (black columns) for ^{252}Cf per 100 fission events and the calculated yields (gray columns) in the *Lagrange* scenario. Theoretical yields are normalized to the total experimental ternary yield. Each fragmentation channel is indicated by the light fragment. The experimental errors (not shown) are less than or of the order of 50%.

^{252}Cf. Two regions of cold fission yields are experimentally observed: one corresponding to large fragment deformations and another one to spherical fragments, like in the case of binary fragmentation. It is worth mentioning that based on the existing experimental data on cold α ternary yields [14]

the first region is expected to contain the main cold fission yields while the second region represents only a few percent of the whole process. Analyzing the structure of the three body potential only few scenarios are possible, all of them related to the initial position of the α particle in the equatorial plane. Only for the Lagrange scenario which corresponds to the α particle situated on the top of the α barrier did we find that the cold α ternary yields of ^{252}Cf are strongly correlated with the cold binary yields of the daughter nucleus ^{248}Cm (see Fig. 9). For all other considered scenarios, adiabatic or based on some excited state in the interfragment ridge well, the α ternary cold fission yields exist mainly for the splittings with one spherical fragment (see Fig. 8). Because of the fact that there are experimental data for both regions, we conclude that only the Lagrange scenario can describe the cold α ternary process. We would like to mention that the cold fission yields depend dramatically on some parameters like diffusivity a. If we choose larger a values for the deformed nuclei than for spherical ones, we can enhance drastically the corresponding yields. Also by choosing larger values for the diffusivity for odd-even fragmentations than for even-even fragmentations, we obtain a larger odd-even effect. We expect the largest yield for odd-even and odd-odd fragmentations. Evidently, such effects must exist for excited fragments when the level density is important. Further experimental data are necessary in order to clarify such effects.

Finally we mention that the cluster model for cold α ternary fission has a number of features suitable for further improvements. These include a modification of the short range part of the M3Y effective interaction which generates the three body interaction potential, inclusion of the preformation factors and level densities near the ground state in the calculated yields, improvement of the description of the penetration process by working with calculated trajectories obtained by solving numerically Eq. (9), and inclusion of dynamical polarization effects into the ground state deformation parameters. Calculations along these lines are in progress.

[1] A. Sandulescu and W. Greiner, J. Phys. G **3**, L189 (1977).

[2] A. Sandulescu and W. Greiner, Rep. Prog. Phys. **55**, 1423 (1992).

[3] A. Sandulescu, S. Misicu, F. Carstoiu, A. Florescu, and W. Greiner, Phys. Rev. C **57**, 2321 (1998).

[4] F. Gönnenwein and B. Borsig, Nucl. Phys. **A530**, 27 (1991).

[5] F.-J. Hambsch, H.-H. Knitter, and C. Budtz-Jorgensen, Nucl. Phys. **A554**, 209 (1993).

[6] A. Benoufella, G. Barreau, M. Asghar, P. Audouard, F. Brisard, T. P. Doan, M. Hussonnois, B. Leroux, J. Trochon, and M. S. Moore, Nucl. Phys. **A565**, 563 (1993).

[7] W. Schwab, H.-G. Clerc, M. Mutterer, J. P. Theobald, and H. Faust, Nucl. Phys. **A577**, 674 (1994).

[8] J. H. Hamilton, A. V. Ramayya, J. Kormicki, W. C. Ma, Q. Lu, D. Shi, J. K. Deng, S. J. Zhu, A. Sandulescu, W. Greiner, G. M. Ter-Akopian, Yu. Ts. Oganessian, G. S. Popeko, A. V.

Daniel, J. Kliman, V. Polhoresky, M. Morhac, J. D. Cole, R. Aryaeinjad, I. Y. Lee, N. R. Johnson, and F. K. McGowan, J. Phys. G **20**, L85 (1994).

[9] G. M. Ter-Akopian, J. H. Hamilton, Yu. Ts. Oganessian, J. Kormicki, G. S. Popeko, A. V. Daniel, A. V. Ramayya, Q. Lu, K. Butler-Moore, M. Morhac, W. Greiner, A. Sandulescu, J. D. Cole, R. Aryaeinjad, N. R. Johnson, I. Y. Lee, and F. K. McGowan, Phys. Rev. Lett. **73**, 1477 (1994).

[10] A. Sandulescu, A. Florescu, F. Carstoiu, W. Greiner, J. H. Hamilton, A. V. Ramayya, and B. R. S. Babu, Phys. Rev. C **54**, 258 (1996).

[11] A. Möller, M. Crönni, F. Gönnenwein, and G. Petrov, in Proceedings of the International Conference on Large Scale Collective Motion of Atomic Nuclei, Brolo, 1996.

[12] F. Gönnenwein, A. Möller, M. Crönni, M. Hesse, M. Wöstheinrich, H. Faust, G. Fioni, and S. Oberstedt, Nuovo Cimento A **110**, 1089 (1997).

[13] A. Sandulescu, A. Florescu, and W. Greiner, J. Phys. G **15**, 1815 (1989).

[14] A. V. Ramayya, J. H. Hamilton, J. K. Hwang, L. K. Peker, J. Kormicki, B. R. S. Babu, T. N. Ginter, A. Sandulescu, A. Florescu, F. Carstoiu, W. Greiner, G. M. Ter-Akopian, Yu. Ts. Oganessian, A. V. Daniel, W. C. Ma, P. G. Varmette, J. O. Rasmussen, S. J. Asztalos, S. Y. Chu, K. E. Gregorich, A. O. Macchiavelly, R. W. Macleod, J. D. Cole, R. Aryaeinjad, K. Butler-Moore, M. W. Drigest, M. A. Stoyer, L. A. Bernstein, R. W. Longheed, K. J. Moody, S. G. Prussin, S. J. Zhu, H. C. Griffin, and R. Donangelo, Phys. Rev. C **57**, 2370 (1998).

[15] GANDS95 Collaboration, A. V. Ramayya, J. K. Hwang, J. H. Hamilton, A. Sandulescu, A. Florescu, G. M. Ter-Akopian, A. V. Daniel, Yu. Ts. Oganessian, G. S. Popeko, W. Greiner, and J. D. Cole, Phys. Rev. Lett. **81**, 947 (1998).

[16] A. Sandulescu, F. Carstoiu, S. Misicu, A. Florescu, A. V. Ramayya, J. H. Hamilton, and W. Greiner, J. Phys. G **24**, 181 (1998).

[17] P. Möller, J. R. Nix, W. D. Myers, and W. J. Swiatecki, At. Data Nucl. Data Tables **59**, 185 (1995).

[18] S. Landowne and J. R. Nix, Nucl. Phys. **A368**, 352 (1981).

[19] H. Esbensen, Nucl. Phys. **A352**, 147 (1981).

[20] T. Kodama, R. A. M .S. Nazareth, P. Möller, and J. R. Nix, Phys. Rev. C **17**, 111 (1978).

[21] M. Brack, J. Damgaard, A. S. Jensen, H. C. Pauli, V. M. Strutinsky, and C. Y. Wong, Rev. Mod. Phys. **44**, 320 (1972).

[22] T. Lederberger and H. C. Pauli, Nucl. Phys. **A207**, 1 (1973).

[23] P. Ring, H. Massmann, and J. O. Rasmussen, Nucl. Phys. **A296**, 50 (1978).

[24] M. Razavy and A. Pimpale, Phys. Rep. **168**, 305 (1988).

[25] L. Landau and E. Lifchitz, *Mechanics* (Mir, Moscow, 1966), Sec. 44.

[26] A. H. Wapstra, G. Audi, and R. Hoecstra, At. Data Nucl. Data Tables **39**, 281 (1988).

[27] M. E. Brandan and G. R. Satchler, Phys. Rep. **285**, 143 (1997).

[28] F. Carstoiu and R. J. Lombard, Ann. Phys. (N.Y.) **217**, 279 (1992).

[29] H. M. A. Radi, J. O. Rasmussen, R. Donangelo, L. F. Canto, and L. F. Oliveira, Phys. Rev. C **26**, 2049 (1982).

[30] A. Sandulescu, A. Florescu, F. Carstoiu, A. V. Ramayya, J. H. Hamilton, J. K. Hwang, B. R. S. Babu, and W. Greiner, Int. J. Mod. Phys. E **7**, 625 (1998).

[31] E. Uegaki, Prog. Theor. Phys. Suppl. **132**, 135 (1998).